

Variant shape growth of nanoparticles of metallic Fe–Pt, Fe–Pd and Fe–Pt–Pd alloys†

Diane Ung,^a Le D. Tung,^b Gabriel Caruntu,^c Dimitrios Delaportas,^d Ioannis Alexandrou,^d Ian A. Prior^{ef} and Nguyen T. K. Thanh^{*gh}

Received 24th December 2008, Accepted 18th February 2009

First published as an Advance Article on the web 10th March 2009

DOI: 10.1039/b823290n

We report the controlled syntheses of Fe–Pt, Fe–Pd and Fe–Pt–Pd nanoparticles having different isolated shapes including sphere, cube, octopod-cube, star, rod, bilobe, tetrahedron, or multipod with size of 5–50 nm. The formation of such a rich variety of shapes was made possible by controlling the synthetic conditions (*e.g.* nature and concentration of the precursors, reaction time, temperature and atmosphere) of a thermal decomposition and reduction of precursors in the presence of surfactants. From the results of the investigation, the possible connection between formation of different shapes and the symmetry of the nuclei as well as the divergent kinetics of particle growth have been examined and discussed.

A Introduction

In the synthesis of nanoparticles (NPs), formation of shapes other than a sphere is usually not energetically favourable because of the high energy gained from different crystal surfaces. Shape-controlled synthesis have already been realised with a few reports recently for some metals,^{1–13} alloys,^{14–20} metal oxides and semiconducting compounds.^{21–23} In addition to the size, control of shape allows the physical and chemical properties of the material to be tuned and the NPs with anisotropic shapes are promising in various applications including catalysts,^{6,10–13} substrates for surface enhanced Raman scattering,^{1,7} magnetic recording media¹⁶ and solar cells.²³ For biomedical applications, shape-variant NPs have immediate utility in biomedical immuno-electron microscopy which allows differentiation by both size and shape simultaneously. Different shapes with tuneable sizes dramatically increase labelling options that are

currently limited to spherical NPs with size below 15 nm.²⁴ This means that many more protein or lipid targets can be labelled simultaneously within a single sample, allowing direct comparison of members of signalling networks or multi-subunit molecular machines.

To form inorganic NPs with anisotropic shapes, one can use either ‘top down’ or ‘bottom up’ strategies. In ‘top down’, the most common method is lithography, by which the different complex shapes of the particles are possible but with size, however, limited to about 100 nm.²⁵ ‘Bottom up’ is based on the preference of anisotropic agglomeration of the atoms during cluster formation which is often achieved by chemical processes in solution assisted by surfactants. Here, the role of the surfactants is not only to prevent aggregation of NPs but also to assist preferential growth of different crystal facets. Although the underlying mechanism of formation of different anisotropic shapes is still a matter of debate, at present, wet chemistry methods have already offered a way to generate NPs with rich variety of shapes such as cube, octahedron, cuboctahedron, polyhedron, tetrahedron, bar, rod, multipod etc. The synthetic strategies, however, at present, still depend very much on experimental trial and error approaches rather than on a systematic design.²² As a result, up till now, the diversity of shape, with high level of homogeneity, has often been achieved using widely different synthetic approaches.

Alloys containing Fe, Pt and/or Pd are a very important class of materials. Crystallographically, they can be either chemically disordered fcc or ordered fct structures. In the latter phase, equimolar FePt and FePd alloys are among those having the highest uniaxial anisotropy (FePt : $K_u = 6.6\text{--}10 \times 10^7 \text{ erg cm}^{-3}$, FePd : $K_u = 1.8 \times 10^7 \text{ erg cm}^{-3}$) which is essential for application of the NPs in information storage and permanent-magnet nanocomposites.^{19,26} Fe–Pt NPs with controlled morphology also have potential in catalysis²⁷ and those with magnetic features could be useful for biomedicine.¹⁹ In addition, it is important to note that NPs based on these alloys provide high stability against oxidation compared with those of magnetic transition metals such as Fe, Co or Ni.

^aDepartment of Chemistry, University of Liverpool, Liverpool, UK L69 7ZD. E-mail: ung@diane@free.fr; Fax: +44 151 7943588; Tel: +44 151 7943486

^bDepartment of Physics, University of Liverpool, Liverpool, UK L69 3BX. E-mail: ltung@liv.ac.uk; Fax: +44 151 794 3441; Tel: +44 151 794 3435

^cAdvanced Materials Research Institute, University of New Orleans, New Orleans, LA, 70148, USA. E-mail: gcaruntu@uno.edu; Fax: +01 504 2803185; Tel: +01 504 2801385

^dDepartment of Electrical Engineering & Electronics, University of Liverpool, Liverpool, UK L69 3GJ. E-mail: ioannis@liverpool.ac.uk; Fax: +44 151 79 44540; Tel: +44 151 7944384

^ePhysiological Laboratory, University of Liverpool, Liverpool, UK L69 3BX. E-mail: iprior@liv.ac.uk; Fax: +44 151 7945461; Tel: +44 151 7945332

^fLiverpool Institute of Nanoscale Science, Engineering and Technology (LINSET), University of Liverpool, Liverpool, UK L69 7ZB

^gThe Davy-Faraday Research Laboratory, The Royal Institution of Great Britain, 21 Albemarle Street, London, UK W1S 4BS. E-mail: ntk.thanh@ucl.ac.uk

^hDepartment of Physics & Astronomy, University College London, Gower Street, London, UK WC1E 6BT

† Electronic supplementary information (ESI) available: TEM images, and compositions analysis of some Fe–Pt, Fe–Pd and Fe–Pt–Pd NPs. See DOI: 10.1039/b823290n

The first chemical synthesis of NPs in this class of alloy was achieved in 2000 by Sun *et al.* for spherical Fe–Pt with tuneable size from 3–10 nm, in the presence of stabilisers oleic acid (OA) and oleyl amine (OLA).²⁸ This method of synthesis was then extended for spherical Fe–Pd and Fe–Pt–Pd NPs.^{29–31} Just recently, with different synthetic approaches, anisotropic shape NPs have been realised, with reports of Fe–Pt nanocubes,^{14–16} nanorods/nanowires,^{17,18} and bilobar structures (Fe–Pt/iron oxide).²⁰ For the Fe–Pd and Fe–Pt–Pd systems, to the best of our knowledge, up till now there has been no report on the synthesis of the anisotropic shape NPs.

In this work, we have carried out comprehensive and systematic studies on the shape variant growth of NPs in the Fe–Pt, Fe–Pd and Fe–Pt–Pd systems. Apart from the already discovered anisotropic shapes (cube, rod, bilobe), we have successfully formed new shapes, including octopod-cube, tetrahedron, multipod, star. The as-synthesised NPs are homogeneous and no further size selection is needed. The formation of such a wide range of shapes from a single synthetic method allowed obtaining some useful information into the growth mechanism of the NPs.

B Experimental

Chemicals

The metallic salts: platinum (II) acetylacetonate Pt(acac)₂ 99.99%, palladium (II) acetylacetonate Pd(acac)₂ 99% and palladium (II) acetate Pd(OAc)₂ 99.9% were purchased from Sigma-Aldrich Ltd, UK. Iron pentacarbonyl Fe(CO)₅ 99.5% was obtained from Acros Organic Ltd, UK. The solvent DCB (1–2 dichlorobenzene anhydrous) 99%, and surfactants OA 99%, OLA 70%, MA (myristic acid) 99%, ACA (adamantanecarboxylic acid) 99%, HDA (hexadecylamine) 90% were purchased from Sigma-Aldrich Ltd, UK. All the reagents were used without further purification.

Syntheses

The syntheses were carried out under oxygen-free condition in a Schlenk line. In a typical synthesis, the precursors containing metallic ions Pt (and/or Pd) and Fe were used in equimolarity (*e.g.* 8.3 mM) in the presence of surfactants (*e.g.* OA and OLA). For Fe–Pt NP system, we used Fe(CO)₅ and Pt(acac)₂ precursors and varying synthetic conditions, *e.g.* changing the concentration of the precursors, their ratios, the nature of the surfactants, their concentrations and reaction atmosphere. For Fe–Pd and Fe–Pt–Pd NP systems, Fe(CO)₅, Pt(acac)₂ and Pd(OAc)₂ or Pd(acac)₂ precursors were used. The volume of solvent DCB was kept at 30 mL. The reaction mixture was degassed three times, stirred at 500 rpm with heating up to 170 °C and kept for 3 h under continuous nitrogen flow over the surface of the reaction mixture.

Transmission electron microscopy (TEM)

The morphology including size and shape of the as-synthesised NPs were studied by TEM. Samples were prepared by diluting the synthesised solution of NPs in toluene and dropped directly onto carbon-coated TEM grids. TEM images were obtained using a FEI Tecnai G² 120 kV TEM and visualised using analySIS software. The dimensions of the NPs and their size

distribution were taken as the mean of a minimum of 500 NPs measured from enlarged photographs using Bersoft Image Measurement 1.0 software, Bersoft Inc, Ontario, Canada.

High resolution transmission electron microscopy (HRTEM)

HRTEM was carried out using a JEOL 4000EX II microscope operated at 400 kV with a resolution limit of 0.14 nm. The crystallographic structure of the particles was examined using the digital diffraction pattern (DDP) produced by applying a fast Fourier transform (FFT) on the HRTEM image scanned directly from the negative at 2400 dpi. This procedure improves the accuracy of the results compared with measuring the lattice spacing and angles directly from the image.

Powder X-ray diffraction (XRD)

The crystal structure and phase purity of NPs were investigated by XRD using an analytical X'Pert system equipped with a graphite monochromator (Cu K α radiation, $\lambda = 1.54056 \text{ \AA}$). Powder samples were dispersed in absolute ethanol and then a colloidal solution of NPs was deposited on a Si(100) substrate followed by the natural evaporation of the solvent. Measurements were performed with a step size of 0.015° in 2 θ with a time per step of 7 s over at least 12 h for each scan. Peak fitting and deconvolution was performed with the ProFit software program whereas the lattice parameters were refined by using the TREOR indexing software. Peak locations and full width at half maximum (FWHM) used to estimate the size of crystalline domains were calibrated against an external Si standard.

Composition analysis

An inductively coupled plasma atomic emission spectroscopy (ICP-AES) (Spectro Ciros^{CCD}) was used to measure the composition of the samples.

C Results

When the synthesis was carried out using Fe(CO)₅ (8.3 mM) and Pt(acac)₂ (8.3 mM) in the presence of surfactant OLA (466 mM) in 30 mL of DCB (dichlorobenzene) at 170 °C under flowing nitrogen atmosphere, we obtained a very homogenous product containing monodisperse spherical NPs. The average particle size is 5.0 ± 0.6 nm (see Fig. 1a). These spherical NPs self-assemble spontaneously and their FFT image shows the arrangement in a typical fcc structure (Fig. 1a, inset).

Under the same synthetic conditions, except that OLA was replaced by OA, we obtained heterogeneous sample that contains NPs of different shapes including spheres, cubes and rods, with sizes in the range of 5–50 nm (ESI, Fig. S1†). These results indicate a very important role for the surfactant in the synthesis of the Fe–Pt NPs. Here, the difference between OA and OLA lies at the functional head group, *i.e.* –COOH for OA instead of –NH₂ for OLA, and presumably this gives rise to the different morphologies obtained.

On the other hand in the presence of a mixture OA and OLA, the synthesis produced homogeneous samples containing only monodisperse nanocubes. These results are in good agreement with those previously reported by the other groups, where Fe–Pt

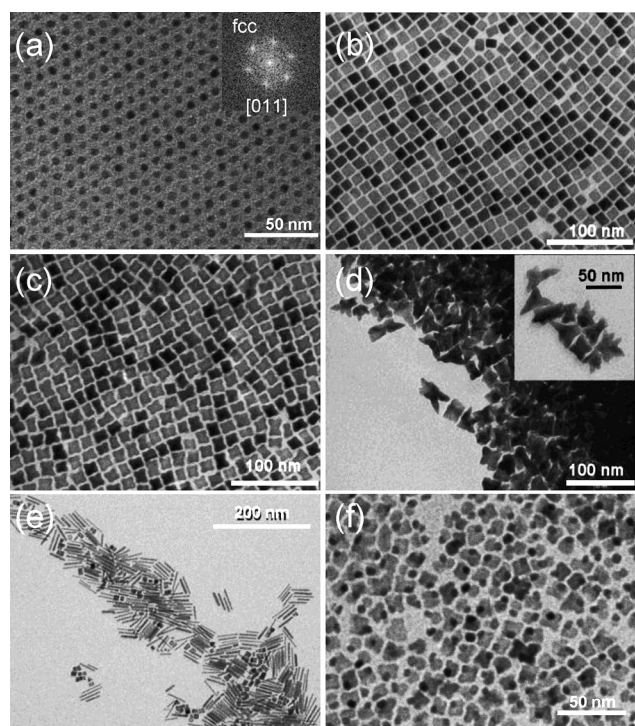


Fig. 1 Formation of spherical (a), cubic (b), octopod-cubic (c), star (d), rod (e) and bilobar (f) Fe-Pt NPs. The image of the Fast Fourier Transform (FFT) of self-assembled NPs in the inset of (a) indicate that they were in a fcc structure. The inset of (d) shows zoom-in view on a few nanostars.

nanocubes with sizes ranging from 4–10 nm were obtained.^{14–16} Here, we have used equimolar amounts of OA and OLA and varied their total concentration. The formation of homogenous nanocubes was possible only with a total concentration of OA and OLA in the range of 133 mM–466 mM (see *e.g.* Fig. 1b). At small concentrations of OA and OLA (16.6 mM), the sample became heterogeneous containing not only nanocubes but also other NPs with ill-defined shape (ESI, Fig. S2†). Whereas, at large concentrations (533 mM), apart from the nanocubes and others with ill-defined shapes; we also observed the appearance of some bilobar NPs (ESI, Fig. S3†).

Besides OA and OLA, other surfactants, including ACA, MA and HAD were also used. In OA and OLA, the tails consist of kinked *cis*-alkenyl chains. On the other hand, ACA has a cyclic hydrocarbon tail, whilst MA and HDA have linear alkyl chains. An equimolar mixture of the two surfactants together at the same total concentration of 266 mM always yielded cube-like NPs but their size depended on the nature of the hydrocarbon chains used in the reaction. When the surfactants were (MA + HDA), (OA + OLA), (ACA + HDA) and (ACA + OLA), nanocubes with corresponding average sizes of 6.7 ± 1.1 , 7.5 ± 1.0 , 8.9 ± 1.0 and 9.2 ± 1.3 nm were obtained (ESI, Fig. S4†). The formation of only nanocubes here means that the nature of the tail in these surfactants does not have a significant role in the preferential growth of the crystalline faces. The change in observed size of the nanocubes could be attributed to different packing of the alkyl chains of surfactants at the particle surface during synthesis. The nanocubes were smaller with MA and HDA having straight alkyl

chains than that with OA and OLA having kinked alkenyl chains. The hydrophobic group in ACA is a sterically-bulky tricyclic hydrocarbon which does not allow well-ordered self-assembly on the surface of the NPs. In the presence of ACA, the size of the nanocubes became even larger.

The reaction atmosphere also influences the morphology of the as-synthesised NPs. We have carried out two different sets of experiments differing only in reaction atmosphere, with the concentration of equimolar amounts of OA and OLA at 466 mM. In the first set, the reaction was carried out in continuous N₂ flow and this yielded homogenous nanocubes with an average size of 9.8 ± 1.6 nm. By contrast, in the second set, the nitrogen flow was cut off after the temperature of reaction reached 170 °C. In this latter condition, homogeneous octopod-cubic NPs with an average size of 13.2 ± 2 nm were formed (Fig. 1c).

When the system was sealed off, the carbon monoxide (CO) generated during the reaction cannot escape but remains in the solution. In this case, the accumulation of carbon monoxide could limit decomposition of Fe(CO)₅ and further nucleation would be reduced in favour of growing bigger NPs. At the same time, the amounts of Fe⁰ and Pt⁰ in the solution also decrease, becoming insufficient to maintain the growth of the cubic NPs. In this case, from the cubic seeds, agglomeration at the corners of the cubes (*i.e.* to form octopod-cubic NPs) would be preferred so as to reduce the surface energy. This is also reinforced by the fact that the corners of each cubic seed are shared by 3 planar surfaces, making them more accessible to incoming atoms or clusters compared to the centre of each planar surface. Since the as-synthesised octopod-cubes are highly monodisperse in size and very homogenous in shape, they can self-assemble themselves into a large micron-sized area (ESI, Fig. S5†).

The concentration of precursors also had an effect on the as-synthesised NPs. Here, one can alter either the total concentration or the ratio Pt(acac)₂ : Fe(CO)₅. With equimolar amounts of Fe(CO)₅ and Pt(acac)₂, it was found that nanocubes can be obtained only when the total concentration of precursors was within the range 16–50 mM. At a total precursor concentration of 12.5 mM, we obtained star-like NPs with an average size of 24.2 ± 6.1 nm (see Fig. 1d). On the other hand, when the total concentration is further diluted to 8.3 mM, the sample is rather heterogeneous containing NPs of ill-defined shape with size of 30 nm or more (ESI, Fig. S6†).

We also investigated the influence of starting Pt(acac)₂ : Fe(CO)₅ ratio on the morphology of the as-synthesised NPs. In these studies, the concentration of Pt(acac)₂ was fixed at 8.3 mM and the concentration of Fe(CO)₅ was varied. It was found that homogenous and monodisperse nanocubes were obtained at the ratio of Fe(CO)₅ : Pt(acac)₂ = 1 : 1, 2 : 1 or 3 : 1 with corresponding average size of 7.5 ± 1 , 8.7 ± 1.5 , 7.6 ± 1.2 nm (ESI, Fig. S4b and S7a,b†). Further increase in the Fe(CO)₅ concentration, *i.e.* Fe(CO)₅ : Pt(acac)₂ = 10 : 1, however, led to the formation of bilobar NPs (see Fig. 1f). These bilobar NPs are quite homogenous with a near-cubic shape, with an average size of 12.5 ± 2 nm. Fig. 1f shows the two lobes very clearly differentiated by size and contrast in the TEM image.

Reaction time also had an effect on the morphology of as-synthesised NPs. A series of syntheses under the same conditions to form nanocubes were stopped by a cold bath at different times. When the temperature reached 170 °C, nanocubes were already

formed, but mixed with nanorods. After 1 hr at the growth temperature of 170 °C, nanocubes were mainly formed with a slight increase in size. After 3–18 h of growth, the NPs were already in the cubic shape. These results indicate that the nucleation step, providing cube-like seeds, took place during the increase of temperature and the growth process continued after the temperature have reached 170 °C. Approximately 1 to 2 h are needed in order to complete the formation of the nanocubes. Based on the above results, we have successfully synthesised nanorods by rapid cooling of the reaction mixture before the formation of nanocubes completed (see Fig. 1e). The presence among the nanorods of small cubic NPs suggests that the rods could be formed by fusion of small cubes. Here, the important factor for rod formation is obviously the cold shock; if the reaction were to carry on, larger cubes would have been formed. The nanorods shown in Fig. 1e have an aspect ratio of ~ 8 , with an average diameter of 5 ± 0.8 nm and mean length of 39.4 ± 8.6 nm. These nanorods have a tendency to be self-aligned which may be due to their magnetic dipole–dipole interaction. Previously, there have been reports of the synthesis of Fe–Pt nanorods for which the reaction was performed either with OA and OLA in a closed autoclave without stirring¹⁸ or in the presence of OLA and ODE (octadecene) with a step increases in temperature to 60, 120 and 160 °C followed by addition of the precursor.¹⁷ These approaches produced the nanorods with diameter of 2–3 nm which is smaller than those obtained from our novel approach based simply on rapid cooling of the reaction.

We have also carried out HRTEM studies on some of the Fe–Pt NPs including the octopod-cubes (Fig. 2), the nanorods (Fig. 3) and the bilobar NPs (Fig. 4) to determine the crystallinity, homogeneity and facet orientations.

The studies revealed the single crystalline nature of the octapod-cubes, because the lattice fringes continued uninterrupted throughout the NPs. In addition, the atomic resolution images showed no trace of surface oxide layer on the NPs. From the HRTEM image, an area was selected to produce the DDP from which one can calculate the lattice spacings. These experimentally determined lattice spacings and the angle between them were then compared to those listed in the EPSRC's Chemical Database.³² From studies of at least 10 different particles, we have verified that the lattice images were consistent with projections of the fcc FePt₃ structure. The particle shown in Fig. 2 is the [100] projection of FePt₃ and the arrows show the direction of the crystallographic planes.

The nanorods appear well dispersed with narrow size distribution (Fig. 3). Even though the magnetic nature of the rods prevents the imaging of lattice fringes over a wide area, realignment of the objective astigmatism at various areas within the grid allowed us to image at least 50 nanorods. The crystalline structure was continuous throughout the length of each nanorod, proving their single crystal structure. A representative lattice image is also included in the inset of Fig. 3.

Figs. 4i and 4iii elucidate the structure of the same bilobar NP at two different values of objective lens defocusing. The lattice spacing revealed is close or slightly below the resolution limit of the microscope. Therefore, near Gaussian defocus, we were able to clearly image the large lobe whilst the spatial frequencies corresponding to the small lobe were smeared out (Fig. 4i). At a certain defocus, we can modify the transfer function of the

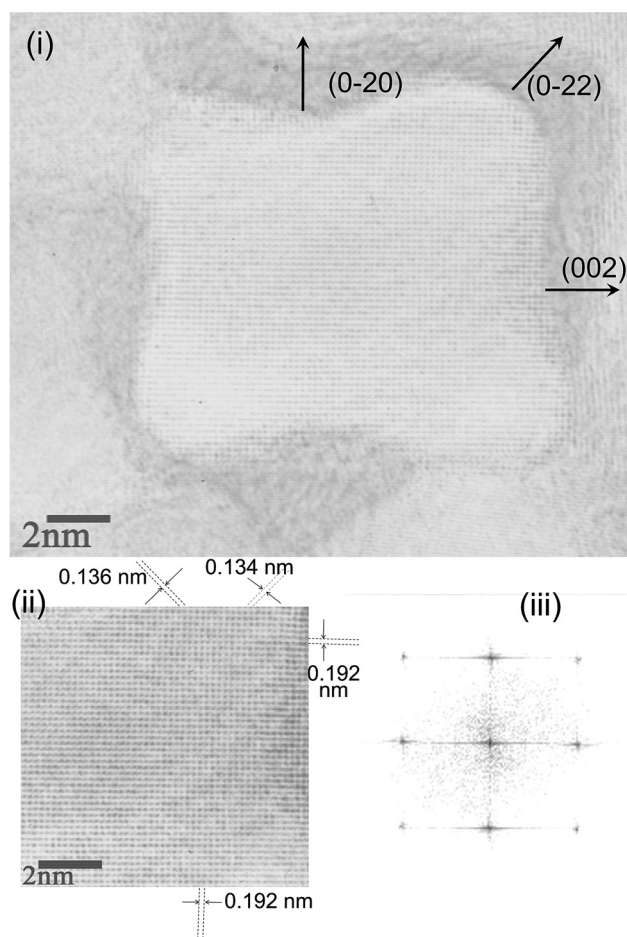


Fig. 2 Fe–Pt octopod-cubes: (i) HRTEM image of an Fe–Pt octopod-cube, (ii) a selected area used to produce the digital diffraction pattern (DDP) shown in (iii), the lattice spacings quoted are those measured directly from the DDP.

microscope and thus faithfully transfer a narrow range of periodicities around those corresponding to the small lobe (Fig. 4iii). We have used selected areas of the two lobes to identify their crystallographic orientation. Figs. 4ii, and 4iv show, respectively,

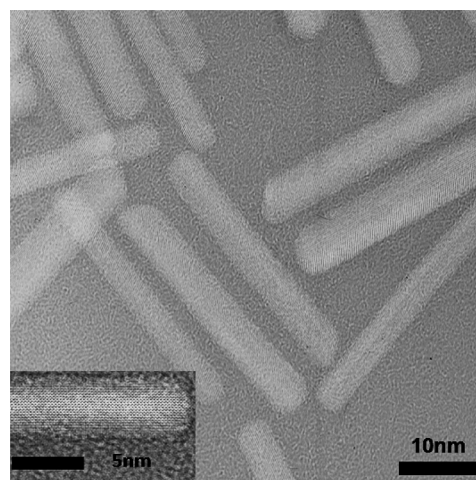


Fig. 3 Fe–Pt nanorods, higher magnification image is shown in the inset.

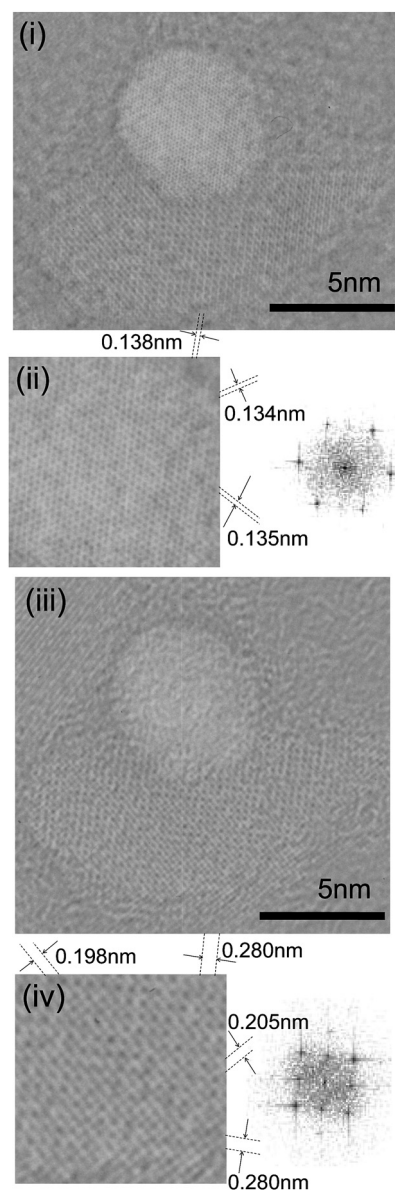


Fig. 4 Fe–Pt bilobars: (i) and (iii) show the same bilobar NPs at two different focus positions; (ii) and (iv) show the corresponding selected areas used for determining the lattice spacings alongside the obtained DDP.

an area of the small and large lobes with the corresponding DDP below them. The lattice spacings quoted are again those measured directly from the DDP. Accordingly, we could identify the small lobe as the [111] projection of Pt but the orientation and phase of the large lobe are ambiguous from the HRTEM image.

For the Fe–Pd system, tetrahedral NPs with size of 15–20 nm (Fig. 5a) were obtained when $\text{Pd}(\text{OAc})_2$ (8.3 mM) and $\text{Fe}(\text{CO})_5$ (8.3 mM) precursors in the presence of OA (133 mM) and OLA (133 mM) were used for the synthesis. It is noted that, we have obtained Fe–Pt nanocubes with an average size of 7.5 ± 1.0 nm, under the same synthetic conditions but when $\text{Pd}(\text{OAc})_2$ was replaced by $\text{Pt}(\text{acac})_2$. From the zoom-in view on each particle, the contrast of the image revealed a three dimensional effect confirming that its real shape is tetrahedral (see inset of Fig. 5a).

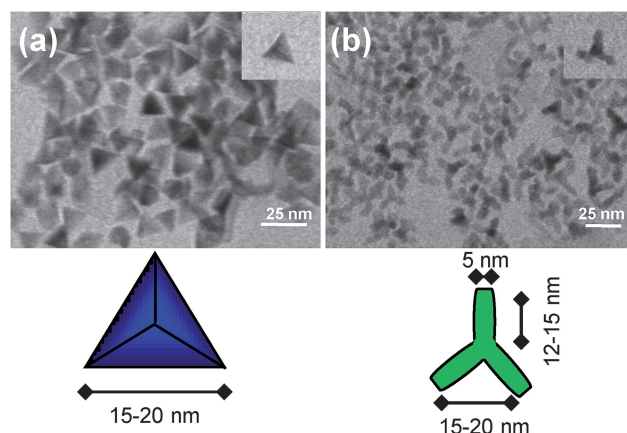


Fig. 5 Formation of triangular-like (a) and multipod-like (b) Fe–Pd NPs. The inset in (a) shows zoom-in view on a selected particle from which the contrast suggests the real shape is tetrahedral. The population of the multipods in (b) is mainly in the form of tri-pods and tetrapods with ‘pod-pod’ distance of 15–20 nm, pod length of 12–15 nm and pod width of 9 nm. The inset in (b) shows zoom-in view on a tri-pod.

We have also investigated the effect of surfactants on the as-synthesised NPs. For this purpose, we have replaced OA and OLA, which have kinked alkenyl chains, with MA and HAD with linear alkenyl chains, keeping the surfactant concentrations the same. The synthesis, however, also yielded NPs of the same tetrahedral shape. The size of the tetrahedral NPs synthesised in the presence of MA and HAD is in the range 13–17 nm which is slightly smaller than that of 15–20 nm obtained for OA and OLA (ESI, Fig. S8†). Thus, similar to the nanocubes mentioned previously, the change in the hydrocarbon chains in these surfactants does not influence the NP shape, but only the size, which again could be associated with the different packing of hydrocarbon chains of surfactants at the particle surface during synthesis.

A change in shape of Fe–Pd NPs from tetrahedral to multipodal was observed either with the addition of the base sodium acetate (Fig. 5b) or when the starting precursor $\text{Pd}(\text{OAc})_2$ was replaced by $\text{Pd}(\text{acac})_2$ (ESI, Fig. S9†). These multipods had a maximum of 4 pods but a few were observed with one or two pods (around 10%). The ‘pod-pod’ distance is in between 15–20 nm, and for the pods, the length was 12–15 nm and average width 5 nm.

For the Fe–Pt–Pd system, when synthesised with $\text{Fe}(\text{CO})_5$ (16.6 mM), $\text{Pt}(\text{acac})_2$ (8.3 mM) and $\text{Pd}(\text{acac})_2$ (8.3 mM) precursors in the presence of OA (133 mM) and OLA (133 mM), multipods were formed of which the majority were again in the form of tri-pods and tetrapods (Fig. 6). This type of morphology still remained when $\text{Pd}(\text{acac})_2$ was replaced by $\text{Pd}(\text{OAc})_2$ (ESI, Fig. S10†). Compared to Fe–Pd, the dimensions of the Fe–Pt–Pd tetrapods were slightly larger. The pods had an average width of 9 nm, length in the range of 15–20 nm and ‘pod-pod’ distance of 20–30 nm.

In Fig. 7, we present the results obtained from powder XRD measurements for some of the NPs. The XRD patterns (Fig. 7a) exhibit diffraction lines which match well with those of a series of Bragg reflections of the standard reference pattern of bulk fcc FePt (JCPDS No. 29-0717). Significant broadening of the peaks

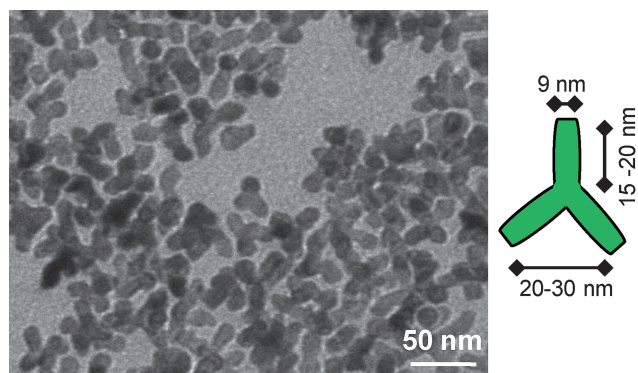


Fig. 6 Formation of multipod-like Fe–Pt–Pd NPs. The population is mainly in the form of tri-pods and tetrapods with ‘pod-pod’ distance of 20–30 nm, pod length of 15–20 nm and pod width of 9 nm.

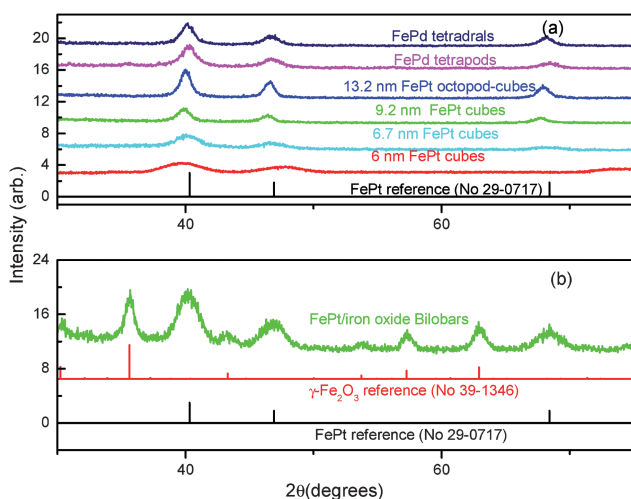


Fig. 7 Powder X-ray patterns of Fe–Pd and Fe–Pt NPs. The patterns in (a) are consistent with the fcc FePt structure (No 29-0717), whereas the pattern in (b) can be indexed by combination of fcc FePt (No 29-0717) and γ -Fe₂O₃ (No 39-1346) phases. The sizes of the cubes as shown in (a) are those determined from TEM images.

can be observed with the decrease in nanocube size. Estimation of the domain size from the full-width at half maximum FWHM of the most intense peak (111) was performed by using the Debye–Scherrer formula and indicated average sizes of the crystallites close to 5.4, 5.6, 8.5 and 12.6 nm. These values are slightly smaller but in good agreement with the corresponding particle size determined from TEM measurements of 6, 6.7, 9.2 and 13.2 nm suggesting that each individual nanoparticle is single crystalline. The calculation of crystallite size for tetrahedral shape NPs gives a value of 14.8 nm close to the mean size observed in TEM images (15–20 nm) and then also suggests that the NPs are mono-crystalline. For Fe–Pd and Fe–Pt–Pd multipods, the same value of 12.3 nm for the mean size of crystallite is obtained. This value is closest to the average pod length as determined from TEM images (12–15 nm for Fe–Pd and 15–20 nm for Fe–Pt–Pd).

For the bilobar NPs, the XRD pattern (Fig. 7b) exhibits well defined diffraction peaks whose intensities and positions suggest

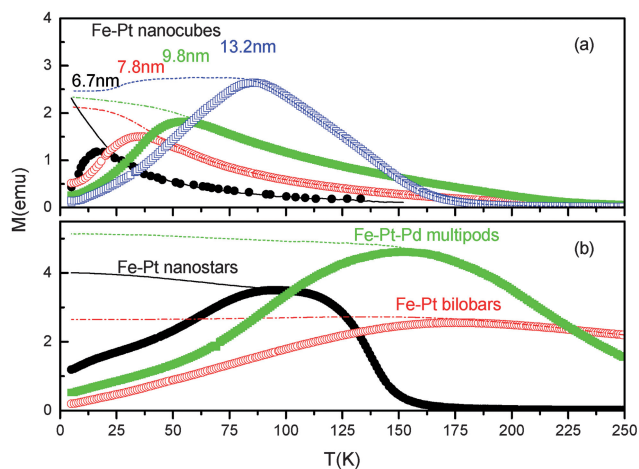


Fig. 8 Zero-field-cooled (ZFC) (symbols) and field-cooled (FC) (lines) magnetisation as a function of temperature for some Fe–Pt, Fe–Pd and Fe–Pt–Pd NPs of different shapes as indicated.

that the sample consists of two phases of the types: FePt (JCPDF No. 29-0717) and γ -Fe₂O₃ (JCPDF No. 39-1346). The calculated cell parameter for the fcc Fe–Pt phase is 3.87(5) Å. Examination of the XRD reflections also shows that the peaks assigned to Fe–Pt are systematically broader than those of γ -Fe₂O₃, which means that the crystallite size of the Fe–Pt is smaller (4.5 nm) than that of the γ -Fe₂O₃ (14.8 nm) which is consistent with the formation of a heterogeneous bilobar structure and the dimension of the lobes observed in TEM.

The results for the zero-field cooled (ZFC) and field-cooled (FC) magnetisation of some NPs as a function of temperature are plotted in Fig. 8. For Fe–Pt nanocubes, the blocking temperature T_B as derived from the peak of the ZFC curve is increasing with increasing the particle size from 16 K for 6.7 nm to 85 K for 13.2 nm particles. The relatively low values of the blocking temperature T_B are consistent with the fact that these nanocubes are crystallised in the disorder fcc phase with low crystalline anisotropy as derived from the powder XRD measurements. The splitting between ZFC and FC curves for all the nanocubes occurs at temperature fairly close to T_B confirming the homogeneity and monodispersity of the samples as seen from the TEM images. For other NPs, the Fe–Pt nanostars have blocking temperature T_B of about 95 K and Fe–Pt–Pd multipods of about 150 K. The Fe–Pt bilobars also have just a single peak on the ZFC curve at about 175 K which is indicative of the fact that the two phases Fe–Pt and γ -Fe₂O₃ are indeed coupled together and so they behave as the single phase NPs.

D Discussion

In syntheses, where the starting concentrations of precursors had the ratio Fe : Pt or Fe : Pd of 1 : 1, the composition of the as-synthesised NPs did vary amongst samples (ESI, Table S1†). From a plot of the composition versus particle size for Fe–Pt (Fig. 9), it can be seen that the NPs had a tendency to be more enriched with Pt when the particle size increases. For Fe–Pd and Fe–Pt–Pd, the concentration of Fe was also low (*i.e.* 14–30% in molarity) in the relatively large NPs. It is noted that, under similar synthetic conditions at 170 °C, in the presence of ligand(s)

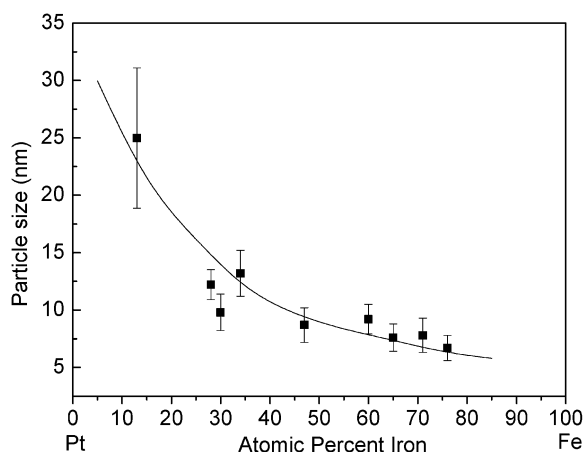


Fig. 9 Composition dependence of particle size for Fe–Pt NPs. Here, the starting concentrations of precursors had the ratio Fe : Pt = 1 : 1 but the composition of as-synthesised Fe–Pt NPs had a tendency to increase the Pt content with increasing the size of the NPs.

(*e.g.* OA and OLA) for Pt(acac)₂ (or Pd(acac)₂), no Pt (Pd) NPs were formed. On the other hand, with the addition of Fe(CO)₅, thermal decomposition can take place giving metallic Fe⁰ atoms. These Fe⁰ atoms, then, can act as a reductant for Pt²⁺ (Pd²⁺) ions and, at the same time, combine with Pt⁰ (Pd⁰) atoms created from the reduction to form the Fe–Pt (Fe–Pd) NPs (see Fig. 10). This reaction pathway is different to the previous method of forming Fe–Pt spherical NPs, where the synthesis was based on the reduction of Pt(acac)₂ by a diol and the decomposition of Fe(CO)₅ in a “polyol process”.²⁸

Formation of NPs involves two steps, nucleation and growth. Our results have given some insight into these processes of NP formation. Temporal separation of these two steps, *e.g.* by making the nucleation period short, would promote subsequent uniform growth on the existing nuclei to form monodisperse NPs.³³ The nucleation process depends very much on the nature and surface energy of the nuclei. Under our synthetic conditions at 170 °C, with only Fe(CO)₅ as precursors, NPs were not formed. This fact indicates the importance of Pt²⁺ (Pd²⁺) in lowering the free energy required for inducing nucleation. The shape of the as-synthesised NPs depends strongly on the symmetry of primary nuclei, which is difficult to predict and control. At the same time, the growth of NPs is also influenced by the rate of aggregation of free metal atoms Fe⁰ and Pt⁰ (Pd⁰) in

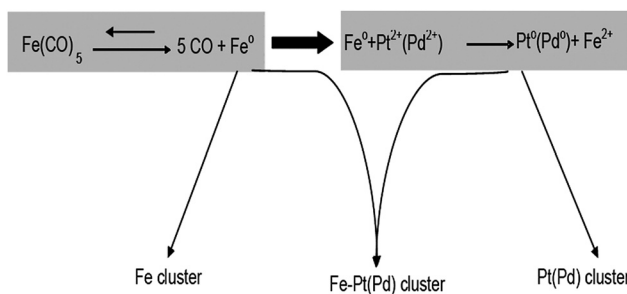


Fig. 10 Proposed mechanism for the formation of the Fe–Pt (and/or Pd) NPs.

the reaction. This rate, in turn, depends on the supersaturated concentration of precursors in solution that is determined by the rate of thermal decomposition of Fe(CO)₅ as well as the reduction of Pt²⁺ (Pd²⁺) to Pt⁰ (Pd⁰). The control of the rate, or supersaturated concentration, allows anisotropic NPs to grow as demonstrated in our synthesis, for instance, by changing the type of precursors, surfactants, precursor concentrations and basicity of the medium.

It was observed that multipods of a similar size can be obtained for both Fe–Pd and Fe–Pt–Pd systems. For Fe–Pd, the synthesis was carried out with the same concentration of Fe(CO)₅ (8.3 mM) and Pd(acac)₂ (8.3 mM). On the other hand, for Fe–Pt–Pd, the total concentration of precursors was double with Fe(CO)₅ 16.6 mM, Pt(acac)₂ 8.3 mM and Pd(acac)₂ 8.3 mM. Furthermore, the multipodal morphology of the Fe–Pt–Pd NPs is almost unchanged when Pd(acac)₂ is replaced by Pd(OAc)₂. Thus, in these cases, the driving force for elongation growth which led to the formation of multipods could be the growth from primary nuclei which have the same symmetry, possibly tetrahedral, in both systems.

The synthesis with Fe(CO)₅ (8.3 mM) and Pt(acac)₂ (8.3 mM) produced Fe–Pt nanocubes of about 7.5 nm. Compared with this, when Pt(acac)₂ was replaced by Pd(OAc)₂ or Pd(acac)₂ (also 8.3 mM), tetrahedral (15–20 nm) or multipod Fe–Pd NPs, respectively, were obtained. The standard oxido-reduction potential of Pd²⁺ to Pd⁰ is 0.915 V which is smaller than that of 1.2 V for Pt²⁺ to Pt⁰. Thus, under the same synthetic conditions, Pd²⁺ ions are more difficult to be reduced than Pt²⁺, resulting in a lower supersaturated concentration, and as a consequence a lower nucleation rate would be expected for Fe–Pd compared with the Fe–Pt system.

With an excess amount of Fe(CO)₅ over Pt(acac)₂, the bilobar NPs were obtained. Here, the origin of this particular morphology may come from the growth occurring in two steps. The first step involves both Pt and Fe atoms, and it leads to the formation of a metallic core, which latter can serve as a seed for a heterogeneous nucleation growth to form a protuberant lobe due to Fe atoms aggregation. At the end of the synthesis, opening of the reaction vial at ambient atmosphere leads to the oxidation of the metallic iron to form the magnetic iron oxide phase. The bilobar feature of the NPs indicates preferential growth from one side of the seed, excluding the possible formation of a core-shell structure. Previously, the use of the Fe–Pt NPs as seeds has been reported for the formation of Fe–Pt/Au heterodimers,³⁴ core-shell structure of Fe–Pt/MnO₃³⁵ and Fe–Pt/CdS.³⁶ In our case, not all of the Fe–Pt NPs serve as seeds for the formation of the bilobar NPs. However, the two populations containing Fe–Pt and the bilobar NPs in the as-prepared sample can be easily separated using a magnet. It is interesting to note that some of the bilobar NPs have grown with a near-cubic shape. With increasing Fe(CO)₅ concentration, the population of the bilobar NPs increases, and the size of the iron oxide moiety also increases. Decreasing the Pt(acac)₂ amount does not significantly change the size of seeds.

It is also interesting to note that, for the Fe–Pd system, very similar multipods were obtained when syntheses with Pd(acac)₂ or Pd(OAc)₂ plus addition of sodium acetate. Thus, the presence of the base in the medium is equivalent to the change of precursors. Here, the base could affect H-bonding interactions in

the aprotic solvent by binding of carboxylic acids as in sodium biacetate or it inhibits the dissociation of Pd(OAc)₂. As a result, it could lead to a lower rate of reduction of Pd²⁺ to Pd⁰ which, in turn, will decrease the concentration of metallic atoms in the medium, and will affect the supersaturation and the rate of the growth process. A definitive mechanistic description of the formation of NPs will require further investigation, particularly of the time-dependence in relation to factors such as precursor concentration, ligands, and solvents.

Conclusions

In summary, we have reported the synthesis of NPs with very rich varieties of shapes, including sphere, cube, octopod-cube, star, rod, bilobe, tetrahedron, and multipods for the isostructural Fe–Pt, Fe–Pd and Fe–Pt–Pd alloys. The results of our comprehensive studies provide some mechanistic insight into the formation of anisotropically shaped NPs, which is presumably connected to the symmetry of the nuclei and the kinetics of growth. In conjunction with spherical NPs, the availability of novel NP shapes will increase the use of these materials in various applications including magnetic recording media and biomedical immuno-electron microscopy.

Acknowledgements

This work was funded by the Biotechnology and Biological Sciences Research Council, BBSRC (BB/E00637X/1), UK. N.T.K.T. and I.A.P. thank the Royal Society for their University Research Fellowships. We thank Donald Bethell, Jane Rees and David G Fernig for very useful discussion; Ian Robinson, Le T. Lu and Daniel Dawson are thanked for technical assistance.

References

- 1 C. J. Murphy, T. K. Sau, A. M. Gole, C. J. Orendorff, J. Gao, L. Gou, E. S. Hunyadi and T. Li, *J. Phys. Chem. B*, 2005, **109**, 13857.
- 2 F. Dumestre, B. Chaudret, C. Amiens, P. Renaud and P. Fejes, *Science*, 2004, **303**, 821.
- 3 F. Dumestre, B. Chaudret, C. Amiens, M. Fromen, M. J. Casanove, P. Renaud and P. Zurcher, *Angew. Chem., Int. Ed.*, 2002, **41**, 4286.
- 4 S. M. Humphrey, M. E. Grass, S. E. Habas, K. Niesz, G. A. Somorjai and T. D. Tilley, *Nano Lett.*, 2007, **7**, 785.
- 5 Y. Zhang, M. E. Grass, J. N. Kuhn, F. Tao, S. E. Habas, W. Huang, P. Yang and G. A. Somorjai, *J. Am. Chem. Soc.*, 2008, **130**, 5868.
- 6 K. H. Park, K. Jang, H. J. Kim and S. U. Son, *Angew. Chem., Int. Ed.*, 2007, **46**, 1152.
- 7 N. Zetsu, J. M. McLellan, B. Wiley, Y. Yin, Z. Y. Li and Y. Xia, *Angew. Chem., Int. Ed.*, 2006, **45**, 1288.
- 8 Y. Xiong, J. Chen, B. Wiley, Y. Xia, Y. Yin and Z. Li, *Nano Lett.*, 2005, **5**, 1237.
- 9 Y. Xiong, H. Cai, B. J. Wiley, J. Wang, M. J. Kim and Y. Xia, *J. Am. Chem. Soc.*, 2007, **129**, 3665.
- 10 H. Lee, S. E. Habas, S. Kwekin, D. Butcher, G. A. Somorjai and P. Yang, *Angew. Chem., Int. Ed.*, 2006, **45**, 7824.
- 11 C. Wang, H. Daimon, T. Onodera, T. Koda and S. Sun, *Angew. Chem., Int. Ed.*, 2008, **47**, 1.
- 12 N. Tian, Z. Zho, S. Sun, Y. Ding and Z. L. Wang, *Science*, 2007, **316**, 732.
- 13 R. Narayanan and M. A. El-Sayed, *J. Phys. Chem. B*, 2005, **109**, 12663.
- 14 V. Nandwana, K. E. Elkins, N. Poudyal, G. S. Chaubey, K. Yano and J. P. Liu, *J. Phys. Chem. C*, 2007, **111**, 4185.
- 15 M. Chen, J. Kim, J. P. Liu, H. Fan and S. Sun, *J. Am. Chem. Soc.*, 2006, **128**, 7132.
- 16 N. Shukla, C. Liu and A. G. Roy, *Mater. Lett.*, 2006, **60**, 995.
- 17 C. Wang, Y. L. Hou, J. M. Kim and S. H. Sun, *Angew. Chem., Int. Ed.*, 2007, **46**, 6333.
- 18 M. Chen, T. Pica, Y. B. Jiang, P. Li, K. Yano, J. P. Liu, A. K. Datye and H. Fan, *J. Am. Chem. Soc.*, 2007, **129**, 6348.
- 19 S. Sun, *Adv. Mater.*, 2006, **18**, 393.
- 20 A. Figuerola, A. Fiore, R. D. Corato, A. Falqui, C. Giannini, E. Micotti, A. Lascialfari, M. Corti, R. Cingolani, T. Pellegrino, P. D. Cozzoli and L. Manna, *J. Am. Chem. Soc.*, 2008, **130**, 1477.
- 21 Y. Yin and A. P. Alivisatos, *Nature*, 2005, **437**, 664.
- 22 Y. Jun, J. Choi and J. Cheon, *Angew. Chem. Int. Ed.*, 2006, **45**, 3414.
- 23 W. U. Huynh, J. J. Dittmer and A. P. Alivisatos, *Science*, 2002, **295**, 2425.
- 24 I. A. Prior, C. Muncke, R. G. Parton and J. F. Hancock, *J. Cell Biol.*, 2003, **160**, 165.
- 25 A. B. D. Brown, C. G. Smith and A. R. Rennie, *Phys. Rev. E*, 2000, **62**, 951.
- 26 D. Weller, A. Moser, L. Folks, M. E. Best, W. Lee, M. F. Toney, M. Schwickert, J. U. Thiele, M. F. Doerner and H. Ku, *IEEE Trans. Magn.*, 2000, **36**, 10.
- 27 T. Toda, H. Igarashi, H. Uchida and M. Watanabe, *J. Electro. Soc.*, 1999, **146**, 3750.
- 28 S. Sun, C. B. Murray, D. Weller, L. Folks and A. Moser, *Science*, 2000, **287**, 1989.
- 29 M. Chen and D. E. Nikles, *J. App. Phys.*, 2002, **11**, 8477.
- 30 S. Kang, Z. Jia, D. E. Nikles and J. W. Harrell, *J. App. Phys.*, 2004, **95**, 6744.
- 31 Y. Hou, H. Kondoh, T. Kogure and T. Ohta, *Chem. Mater.*, 2004, **16**, 5149.
- 32 D. A. Fletcher, R. F. McMeeking and D. J. Parkin, *J. Chem. Inf. Comput. Sci.*, 1996, **36**, 746.
- 33 V. K. LaMer and R. H. Dinegar, *J. Am. Chem. Soc.*, 1950, **72**, 4847.
- 34 J. S. Choi, Y. W. Jun, S. I. Yeon, H. C. Kim, J. S. Shin and J. Cheon, *J. Am. Chem. Soc.*, 2006, **128**, 15982.
- 35 S. Kang, G. X. Miao, S. Shi, Z. Jia, D. E. Nikles and J. W. Harrel, *J. Am. Chem. Soc.*, 2006, **128**, 1042.
- 36 J. Gao, B. Zhang, Y. Gao, Y. Pan, X. Zhang and B. Xu, *J. Am. Chem. Soc.*, 2007, **129**, 11928.